Realising bio-inspired impact damage-tolerant thin-ply CFRP Bouligand structures via promoting diffused sub-critical helicoidal damage

Lorenzo Mencattelli[a], Silvestre T. Pinho[a]

[a]*Department of Aeronautics, Imperial College London South Kensington, SW7 2AZ, UK*

Abstract

In this work, we manufactured bio-inspired thin-ply Carbon Fibre Reinforced Plastic (CFRP) laminates, mimicking the helicoidal architecture of the mantis shrimp's dactyl club periodic region, with the smallest inter-ply (pitch) angle in the literature (2.5°), thus better mimicking the actual micro-structure of the dactyl club. We conducted Low Velocity Impact (LVI) tests on a wide range of pitch angles (2.5°, 5°, 10°, 20°, 45°), thus demonstrating that decreasing the pitch angle leads to a progressively smoother double helicoidal evolution of damage, reduces delamination areas, diffuses sub-critical damage, and enhances damage tolerance. We then conducted Compression After Impact (CAI) tests, thereby demonstrating that the residual strength and failure strain are preserved as the pitch angle is reduced, even though there is a steep decrease in the proportion of 0°-plies (plies aligned with the loading direction) as the pitch angle decreases. Via detailed modelling, we then developed and proposed an explanation for why very small pitch angles are required to achieve the beneficial damage mechanisms exhibited by biological Bouligand structures.

Keywords: Thin-ply, Bouligand, Helicoidal, LVI, CAI, damage tolerance

1. Introduction

Non-standard lamination sequences inspired by naturally-occurring impact-resistant micro-structures, such as Bouligand [1] structures (Fig. 1a), have been investigated in the past years in order to improve the resistance of Fibre Reinforced Plastic (FRP) (and specifically Carbon Fibre Reinforced Plastic (CFRP)) lami-

Email addresses: l.mencattelli@imperial.ac.uk (Lorenzo Mencattelli), silvestre.pinho@imperial.ac.uk (Silvestre T. Pinho)

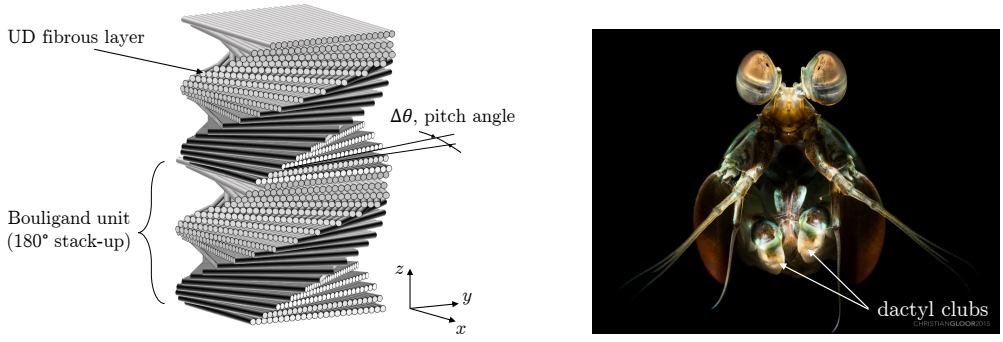

(a) (b)

Figure 1: (a) Schematic of Bouligand micro-structure; (b) photograph of the mantis shrimp (*Odontodactylus scyllarus*) [11].

nates to out-of-plane loads [2–10]. Significant progress has been made in our understanding of Bouligand structures [2–10]; however, we have not yet been able to fully exploit this type of highly damage tolerant micro-structure in engineering solutions.

Bouligand-featured structures can be found in a variety of animals, including the mantis shrimp (*Odontodactylus scyllarus* in Fig. 1b [11]). The so called periodic region of the mantis shrimp's dactyl club micro-structure consists of several repetitions of the Bouligand unit, stacked up along the thickness direction [12]. Each Bouligand unit (Figure 1a) contains a helicoidal layup with very small inter-ply (pitch) angles $\Delta\theta$ (from 6.2° to 1.6° [4]) for a total rotation of 180° inside each unit.

By analysing the coronal cross section of an impacted club (Figure 2), we observe an interesting mechanism of failure under impact: several cracks nest inside each

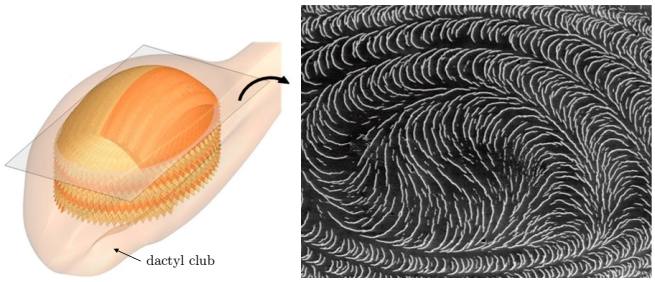

Figure 2: SEM micrography of a coronal cross section of the dactyl club showing cracks (in white) nesting in the Bouligand units of the periodic region of the club (adapted from Weaver *et al.* [12]) and Suksangpanya *et al.* [9] .

Table 1: Experimental tests conducted in previous studies on Bouligand FRP composites [2–8].

Author(s)	Baseline material	Configurations and pitch angles $\Delta\theta$	Sample thickness [mm]	Periodicity	Test(s)
		UD			
Apichattrabrut *et al.*[2]	CFRP (NCT304-1)	±45°	6.35 (40 layers)		Tension, Bending, Ballistic
		10° (S)		2	
		QI			
Cheng *et al.* [3]	GFRP (DA409U/S2-glass)	7.8° (S & NS)	4.5-5 (24 layers)	2	Short and long beam bending
		16.4° (S)		2	
		UD			
		QI			
Grunenfelder *et al.* [4]	CFRP (CYCOMS320-1)	7.8° (S)	6.5 (48 layers)	2	High energy Impact (100 J), CAI
		16.3° (S)		4	
		25.7° (S)		6	
		CP			
Shang *et al.* [5]	CFRP (T700/2510)	10° (NS)	0.88-1.52 (11 & 19 layers)	1	Quasi-static indentation
		18° (NS)		1	
		QI			
Pinto *et al.* [6]	CFRP (T800/M21)	15° (S)	26 layers	2	Tension, LVI (30 J), CAI
		15° (NS)		2	
		CP			
		QI			
Ginzburg *et al.* [7]	CFRP (T800/M21)	6° (NS)	4 (32 layers)	1	LVI (40-80 J), CAI
		12° (NS)		2	
		12° (S)		2	
		CP			
Liu *et al.* [8]	CFRP (T700/2510)		1.52 (19 layers)		Quasi-static indentation
		10° (NS)		1	
UD - Unidirectional	CP - Cross ply	QI - Quasi-isotropic	NS - Non Symmetrical	S - Symmetrical	

unit, growing in a helicoidal pattern, remaining parallel to the local fibre orientation mainly via cracking matrix, leaving fibres mostly undamaged [12]. The accumulation of the highly diffused sub-critical damage (visible in Figure 2) allows biological Bouligand structures to withstand several impacts while retaining more of their undamaged mechanical properties.

The attempts to exploit the enhanced impact damage tolerance of biological Bouligand arrangements in CFRP and Glass Fibre Reinforced Plastic (GFRP) structures led to significant progress [2–8]. In some studies (see Table 1), FRP Bouligand laminates outperformed conventional laminates under out of plane loadings [2–4, 6, 7]. In other studies, [5, 8] (Table 1), CFRP Bouligand laminates achieved enhanced load bearing capability, albeit with a more brittle response and different failure mechanisms than those observed in the biological Bouligand microstructures. The latter has been also observed in other studies on CFRP Bouligand laminates [4, 7]. Finally, in the study conducted by Ginzburg *et al.* [7] (Table 1),

the residual compressive properties due to high impact energies (80 J) of CFRP Bouligand microstructures was found to be better than the corresponding quasi-isotropic; however, the impact performances at lower impact energies (40 J) of CFRP Bouligand laminates fell behind those of conventional configurations.

One of the challenges that needs overcoming in order to achieve enhanced impact damage tolerance in Bouligand CFRP structures is achieving small pitch angles $\Delta\theta$ and large number of Bouligand unit repetitions through the thickness of the laminate, given the current standard pre-preg thicknesses ($\sim$0.1 mm). For instance, the smallest pitch angle $\Delta\theta$ published to date in the literature on CFRP Bouligand structures is 6° [7] (Table 1), while in natural Bouligand microstructures pitch angles $\Delta\theta$ of 1.6° have been observed [4]). Small pitch angles ($\Delta\theta < 7.8°$) have been so far manufactured only in non symmetrical configurations [5, 7, 8] possibly resulting in a detrimental effect on the performance of the laminate due to residual thermal stresses [6]. Moreover, while biological Bouligand structures contain many repetitions of the Bouligand unit with small pitch angles $\Delta\theta$, engineered Bouligand structures with small pitch angles ($\Delta\theta < 15°$) in the literature have never exceeded two repetitions [2–8]).

In view of this, we devised an original experimental and modelling study to investigate thin-ply Bouligand structures under Low Velocity Impact (LVI) and Compression After Impact (CAI). For the first time in the literature:

(i) thin-ply CFRP pre-preg with a thickness down to 0.024 mm are used to manufacture Bouligand CFRP laminates;

(ii) CFRP symmetric laminates are manufactured with very small pitch angles $\Delta\theta = 2.5°$, in the range of the pitch angles observed in naturally-occurring Bouligand structures;

(iii) a wide range of pitch angles ($\Delta\theta = 2.5°, 5°, 10°, 20°$ and 45°) are explored and compared, where all laminates are symmetric, with the same nominal thickness and loaded under the same loading conditions;

(iv) trends are drawn on the effect of the pitch angle $\Delta\theta$ on the mechanical and damage properties of thin-ply CFRP Bouligand structures under LVI and CAI tests;

(v) it is shown that is possible to achieve enhanced impact damage tolerance with thin-ply Bouligand CFRP structures and small pitch angles $\Delta\theta = 2.5°$;

(vi) an understanding is developed, via a detailed analysis that uses numerically-obtained stress fields, on the role of the pitch angle $\Delta\theta$ on the LVI performances of thin-ply CFRP Bouligand structures;

(vii) conclusions are drawn on the role of various stress components in promoting matrix cracking and delamination, and how this depends on the pitch angle;

(viii) an understanding is developed on the role of the pitch angle $\Delta\theta$ on the propagation of matrix cracks forming at the back face of thin-ply CFRP Bouligand laminates under impact; and

(ix) conclusions are drawn on why very small pitch angles are required with thin-ply CFRP to achieve the beneficial damage mechanisms exhibited by biological Bouligand structures.

The novelty highlighted above, together with the progressive use of automated tow/tape placement in large-scale engineering applications, provides a pathway for the large-scale use of Bouligand microstructures in industrial practice.

2. Experimental Methods

2.1. Manufacturing

We designed five different Bouligand configurations, with pitch angles $\Delta\theta = 2.5°, 5°, 10°, 20°$ and 45°. All configurations have the same nominal thickness with a total of 146 plies, and are all symmetric with respect their mid-plane. We decided to study symmetric laminates in order to avoid the in-plane/bending coupling of an asymmetric lay-up ($\mathbf{B} \neq 0$), which depends on the pitch angle. Therefore, by using

Table 2: Samples specifications for LVI and CAI tests (Mean ± STD).

$\Delta\theta$	Stacking sequence	n°of samples	thickness [mm]	n°of plies	Energy [J]	Impact height [mm]
2.5°	$[0°/2.5°/5°/\ldots/180°]_s$	3	3.56 ± 0.02	146	11.94 ± 0.08	221.29 ± 1.78
5°	$[0°/5°/10°/\ldots/360°]_s$	1	3.57	146	11.96	221.66
10°	$[0°/10°/20°/\ldots/720°]_s$	1	3.60	146	12.06	223.51
20°	$[0°/20°/40°/\ldots/1440°]_s$	1	3.52	146	11.79	218.51
45°	$[0°/45°/90°/\ldots/3240°]_s$	1	3.51	146	11.75	217.77

a symmetric laminate, we can better relate the findings of this work to the pitch angle $\Delta\theta$ directly. Table 2 shows the stacking sequence of each configuration. We considered the $\Delta\theta = 45°$ configuration as the reference configuration in this study since it most closely matches a quasi-isotropic laminate used in engineering practice.

We manufactured samples using Skyflex USN20A, a unidirectional thin-ply pre-preg (20 gsm). The very low thickness of Skyflex USN20A has allowed to reach, for the first time in the literature, extremely low pitch angles $\Delta\theta = 2.5°$ yet maintaining reasonable laminate thicknesses (~ 3.5 mm). The ply-level and the constituents properties of Skyflex USN20A are reported in Tables 3 and 4, respectively. We used an automatic cutting table to cut each ply at the desired angle. We ensured excellent alignment during the lay-up procedure by means of an alignment mould with pin holes [13]. We cured the samples in the same autoclave cycle according to the pre-preg manufacturer's recommendations. After curing, we cut the plates to their final dimensions (150 mm long and 100 mm wide [14, 15]) using a water-jet cutter. Finally, we scanned each sample in an immersion tank with a Ultrasonic C-Scan in order to verify that there were no defects. The details of the manufactured samples are reported in Table 2.

Table 3: Elastic properties of the Skyflex USN20A plies [26] and its constituent.

E_{11}	$E_{22} = E_{33}$	$\nu_{12} = \nu_{13} = \nu_{23}$	$G_{12} = G_{13} = G_{23}$
101.7 GPa	6.0 GPa	0.3	2.4 GPa

Table 4: Constituents properties of Skyflex USN20A [26, 27].

Mitsubishi Rayon TR30S 3K		SK Chemicals K50	
Fibre diameter, (ϕ_{f})	6.8 µm	Young's modulus, E	3.35 GPa
Tensile modulus, (E_{f1})	235 GPa	Shear modulus, G	1.21 GPa
Compression modulus, (E_{f2})	13 GPa	Poisson's ratio, ν	0.38
Shear modulus, (G_{f12})	15 GPa	Density (cured), ρ	1.30 g/cm^3
Poisson's ratio, (ν_{f12})	0.2		
Fibre density, (ρ_{f})	1.79 g/cm^3		
Tensile failure strain, (ε_{f})	1.9 %		

Our goals were to:

(i) characterize the $\Delta\theta$=2.5° configuration because it is the one that better mimics the features of naturally-occurring Bouligand microstructures, and

(ii) investigate the effect of pitch angle $\Delta\theta$ on various characteristics of the response, i.e. to understand how quantities such as projected delamination area during impact correlate with pitch angle.

For goal (i), we manufactured 3 identical samples with pitch angle $\Delta\theta$=2.5° for impact and compression after impact testing. For goal (ii), we manufactured 4 further samples, with pitch angles $\Delta\theta$=5°, 10°, 20° and 45° respectively, also for impact and compression after impact testing.

With regards to goal (ii), note that we do not have specimen repetitions for $\Delta\theta$=5°, 10°, 20° and 45° and hence we will not be able to characterize the scatter for these configurations. However, we have seven specimens whose test results can be used to carry out statistical hypothesis tests on whether correlations between different measurements and pitch angle exist, which is our goal.

2.2. Testing methods: LVI and CAI

We conducted LVI tests using a drop-weight tower (Instron CEAST 9350) following the testing procedure ASTM D7136/D7136M [14]. We kept the impactor mass (5.5 kg) and geometry (hemispherical tip, 8 mm radius) constant in each

test. Plates were simply supported by four rubber pins [14]. To achieve a reasonable amount of damage, we impacted each sample with an impact energy per unit thickness of 3.35 J/mm (Table 2). The impactor reached the laminates with an average velocity of 2.08 m/s. We conducted post-impact damage analysis of the samples by means of visual inspections and ultrasonic C-scans to investigate the distribution of damage, the delamination extent and the projected delamination area. The latter was evaluated by post-processing the C-scan images in Figure 13 (see supplementary material). The image analysis comprises the following steps: (i) grey scale transformation and binarisation of the C-scan images (the threshold for discretisation of black (no-damage) and white (damage) pixels was the same for each sample); (ii) scaling of the pixel dimension to millimetre; and (iii) counting of the white pixels and calculation of the projected delamination area.

We performed CAI tests following the testing procedure ASTM D7137/D7137M [15]. Samples were loaded with a constant displacement rate of 1.25 mm/min using a 250 kN load cell Instron machine. We instrumented each sample with four strain gauges [15], two on the impacted side and two on the back face in order to monitor strains during the test, to verify that the initial alignment of the sample was within acceptable bounds [15] and that global buckling did not occur. In addition, we used 3D digital image correlation on the impacted surface to verify that global buckling did not occur during CAI.

3. Results: LVI and CAI

For the LVI tests, Table 5 shows the peak load, corresponding displacement and absorbed energy for each pitch angle $\Delta\theta$. Figures 3a and 3b respectively show the Force v.s. Time and Force v.s. Displacement curves for all the samples tested. The $\Delta\theta = 2.5°$ response (Figures 3a and 3b) shows a region with a progressive reduction in stiffness until just before the load drop. For $\Delta\theta = 5°, 10°, 20°$ and $45°$, this region does not exist and the linear-elastic behavior is followed by sudden load-drops of increasing magnitude as the the pitch angle $\Delta\theta$ increases. Based

Table 5: Peak force, displacement at peak force, and absorbed energy of LVI tests. Results for $\Delta\theta = 2.5°$ are presented in terms of Mean ± STD.

$\Delta\theta$	Peak force [kN]	Displacement at peak force [mm]	Absorbed Energy [J]
2.5°	5.62 ± 0.092	4.13 ± 0.25	7.1 ± 1.03
5°	4.72	3.26	7.3
10°	5.37	3.16	6.8
20°	5.35	3.23	8.0
45°	4.96	3.06	7.9

on the samples tested in this work, i.e. 3 samples for $\Delta\theta = 2.5°$ and one sample for each one of the other configurations, the $\Delta\theta = 2.5°$ configuration showed a 13.3% higher peak force and a 34.9% higher peak displacement than the $\Delta\theta = 45°$ configuration.

Figure 4 illustrates the three-dimensional representation of the C-Scan images of the impacted samples, representing the delamination damage for each configuration $\Delta\theta$ (see supplementary videos and 2D C-Scan images). The coloured regions represent the delamination areas with different colours associated to different ply-interfaces. Figure 4 shows that reducing the pitch angle $\Delta\theta$ leads to a progressively smoother double helicoidal distribution of damage. Figure 4f shows that, while in the $\Delta\theta = 2.5°$ configuration the through-the-thickness distribution of delaminations is approximately uniform, in the $\Delta\theta = 45°$ configuration they are distributed in a "step-wise" manner (with big jumps occurring only at specific locations across the thickness).

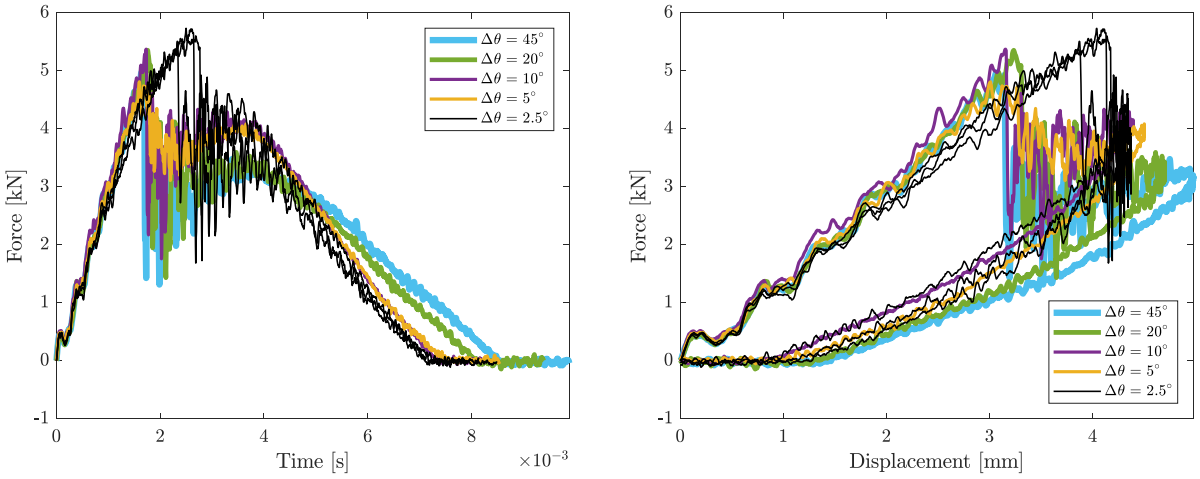

(a) Force v.s.Time (b) Force v.s Displacement

Figure 3: LVI Force v.s. Time and Force v.s. Displacement for $\Delta\theta = 2.5°$, 5°, 10°, 20° and 45°.

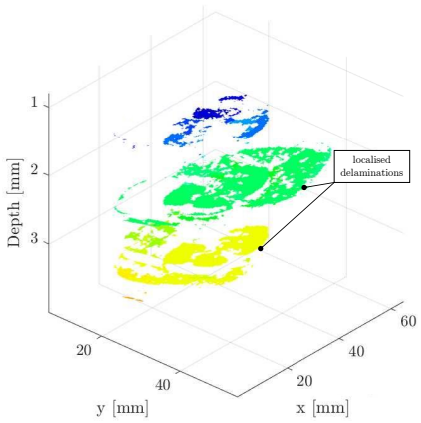

(a) $\Delta\theta = 45°$

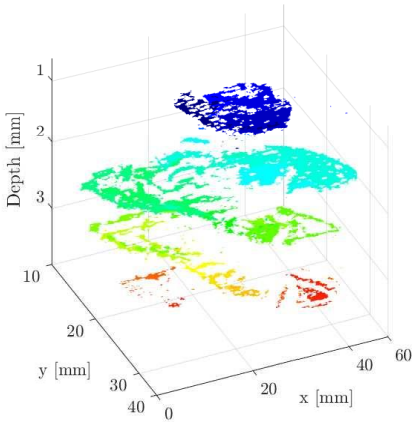

(b) $\Delta\theta = 20°$

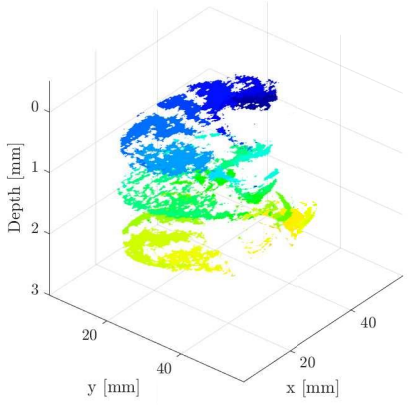

(c) $\Delta\theta = 10°$

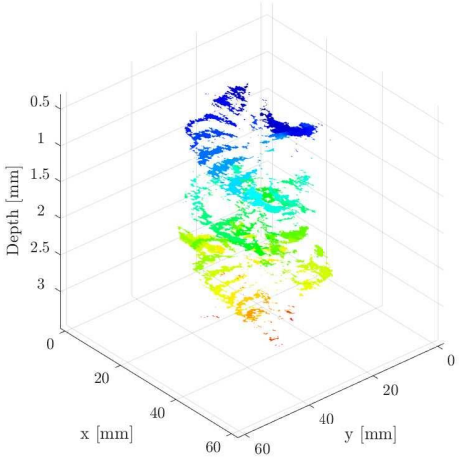

(d) $\Delta\theta = 5°$

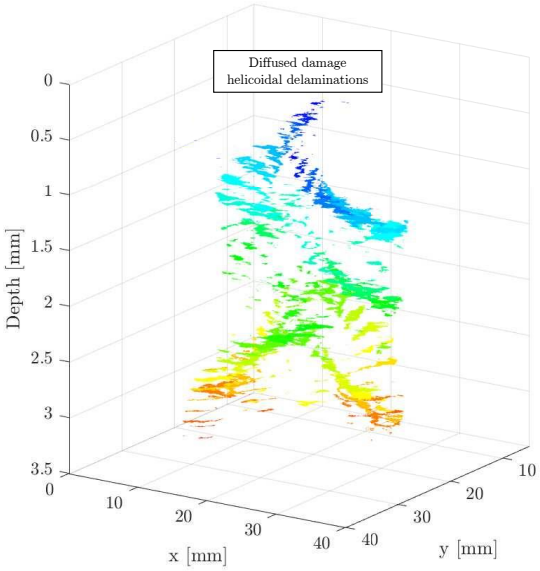

(e) $\Delta\theta = 2.5°$ Sample 1

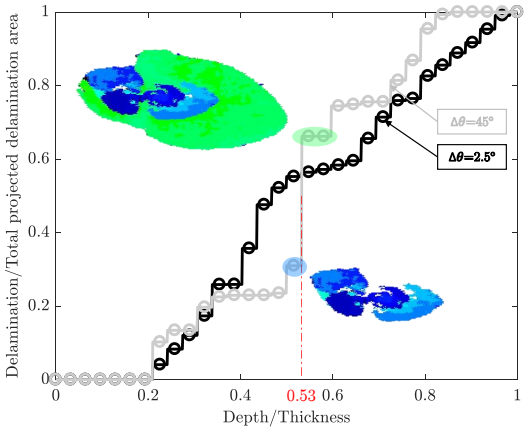

(f) Distribution of delaminations

Figure 4: (a-e) Three-dimensional representation of Ultrasonic C-Scans for configurations with different pitch angles $\Delta\theta$. (f) Through-the-thickness distribution of delaminations in the $\Delta\theta = 2.5°$ (Sample 1) and $\Delta\theta = 45°$ configurations.

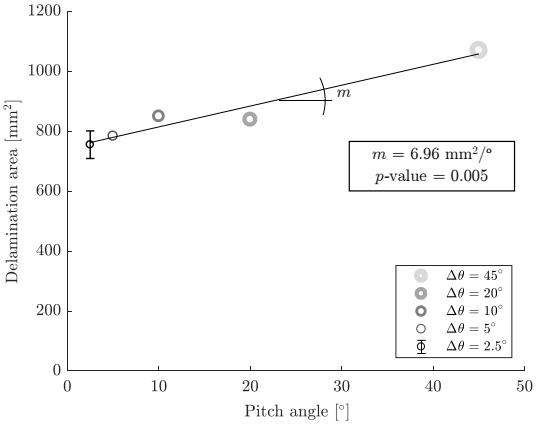

(a)

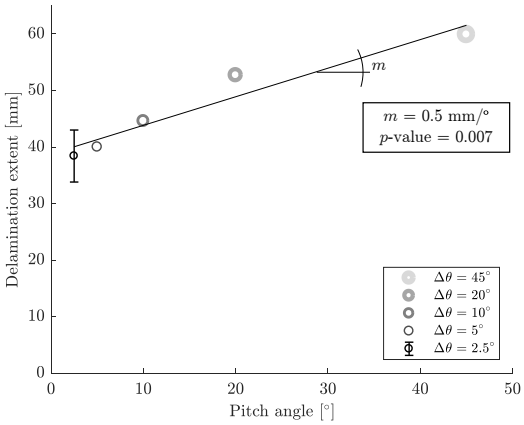

(b)

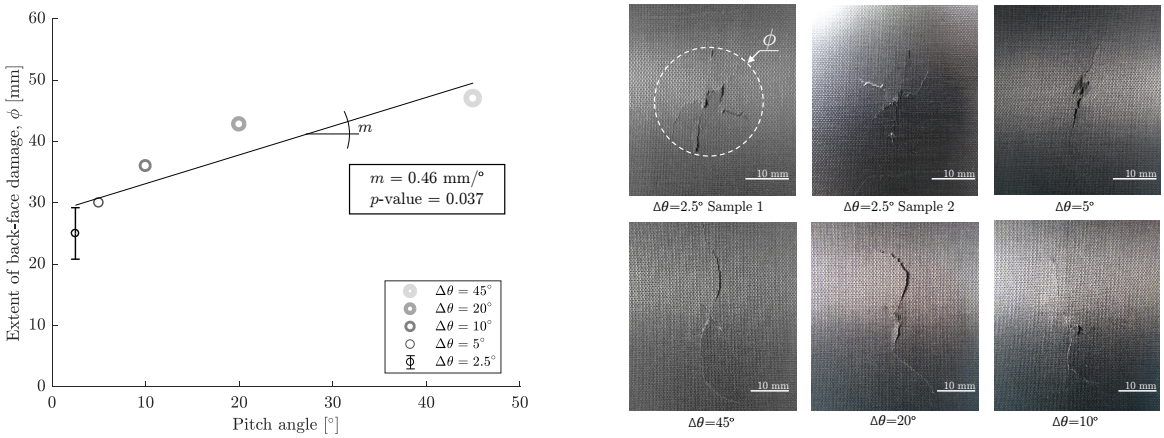

(c) (d)

Figure 5: Effect of the pitch angle $\Delta\theta$ on (a) projected delamination area, (b) delamination extent and (c) extent of back-face damage, ϕ (LVI). (d) Damage at the distal face, showing fibre failures and splitting.

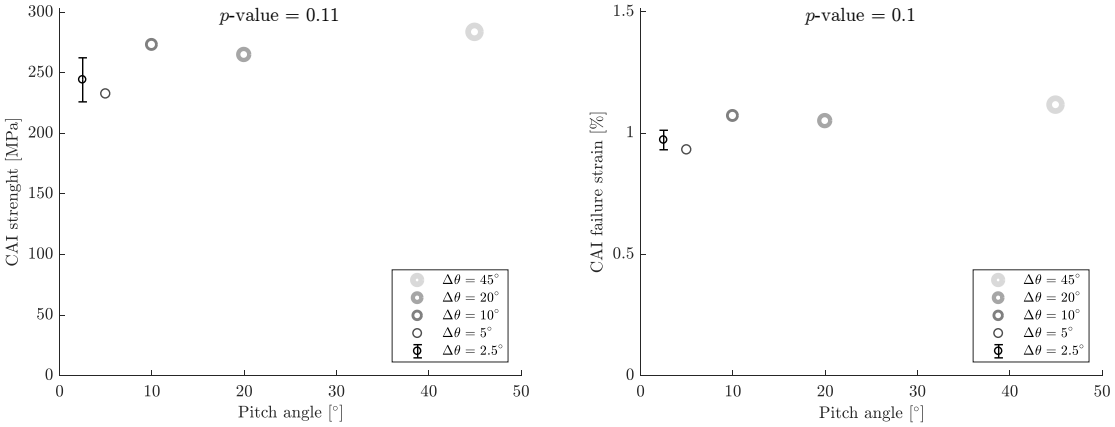

(a) (b)

Figure 6: (a) CAI strength and (b) CAI failure strain for all pitch angles $\Delta\theta$ showing no statistically-significant trends.

We used a least-square linear regression model to calculate trendlines for the effect of the pitch angle $\Delta\theta$ on the total projected delamination area, delamination extent and back face damage (Figures 5a-5c). We performed a calculation of the p-values associated to the slope m of each trendline in order to assess their statistical significance. The value of p corresponds to the probability of the trendline to have a zero slope ($m = 0$) given the experimental data measured. As is common in the literature, we set the threshold value $p \leqslant 0.05$ to conclude that a certain slope is non-zero with sufficient statistical significance.

Based on the samples tested in this work, i.e. 3 samples for $\Delta\theta = 2.5°$ and one sample for each one of the other configurations, Figure 5 shows that reducing the pitch angle $\Delta\theta$ leads to a statistically-significant decrease in total projected delamination area (with a global reduction of 29.4% between $\Delta\theta = 2.5°$ and $\Delta\theta = 45°$), in delamination extent (35.8% decrease) and in extent of back-face damage (46.8% decrease).

Figure 6a and 6b respectively show the CAI strength and failure strain of all the different configurations. The pitch angle $\Delta\theta$ did not show a statistically-significant effect on the residual properties after impact ($p > 0.05$) and all configurations showed similar values of residual CAI strength and failure strain.

4. Discussion

4.1. On the enhanced impact damage tolerance of thin-ply CFRPs Bouligand laminates

As the pitch angle $\Delta\theta$ decreases, the damage due to impact follows an increasingly better-defined double helicoidal (Figure 4), and is more equally-spread across the thickness (with smaller delaminations at more interfaces, Figure 4f). The smooth and highly diffused double helicoidal delamination pattern in the $\Delta\theta = 2.5°$ (Figure 4e) correlates with a substantial increase in displacement at peak load (Figure 3b) and in the energy dissipated prior to the peak load (related to the non-linear region before the peak load in Figure 3b). Therefore, reducing the pitch angle to very small values, down to $\Delta\theta = 2.5°$, leads to higher damage tolerance via a significant sub-critical accumulation of damage.

For $\Delta\theta = 2.5°$, Figure 3a shows sub-critical damage accumulation before the peak load. The low impact energy used in the tests is not likely to have caused fibre failure in the bulk of the laminate at this stage of the test; fibre failure did occur at the distal face (Figure 5d) later in the test, and is related to the load drop visible in Figures 3a and 3b. Therefore, we surmise that the sub-critical damage is the result of the double helicoidal matrix crack and delamination pattern.

Regarding the load drop due to the fibre failure at the distal face mentioned, Figure 3b shows that this occurs at larger displacements for $\Delta\theta = 2.5°$. Therefore, there is also a correlation between the formation of the double helicoidal damage pattern and the delay in fibre failure at the distal face.

Table 5 shows that decreasing the pitch angle $\Delta\theta$ leads to similar dissipated energies. This was achieved via an increasing amount of diffused sub-critical helicoidal damage as the pitch angle decreases. Therefore, by decreasing the pitch angle, it is possible to preserve the energy dissipation capability of the structure via dissipating at a sub-critical level rather than via the activation of catastrophic failure mechanisms (such as the large localised delaminations and extensive fibre breaks observed in $\Delta\theta = 20°$ and $45°$, see Figures 4 and 5).

4.2. On the effect of the pitch angle $\Delta\theta$ on the distribution of sub-critical damage

4.2.1. Role of τ_{13} and τ_{23} on the failure mechanisms in LVI tests

In Section 4.1, we observed that smaller pitch angles lead to an increasingly better-defined double helicoidal damage pattern (Figure 4) and a more homogeneous distribution of delaminations (Figure 4f). In this section we explore the reasons why this may happen.

We know that, during an impact on a composite laminate, the first damage to form is typically matrix cracking; matrix cracks may start in the bulk of the laminate due to shear stresses (shearing cracks), and from the distal face due to bending tensile stresses (bending cracks) [16]. In thin-ply CFRP laminates, shearing cracks and bending cracks do not interact until after fibre failure at the distal face has occurred [17, 18]. In addition, the helicoidal damage experimentally observed in Figure 4 expands around the mid-plane of the laminate, where shearing cracks are expected. Using a combined experimental and analytical approach, Choi *et al.* [16] showed that the shear stress distributions τ_{13} and τ_{23} play a major role in the failure of CFRP laminated composites subjected to low velocity impact. Therefore, we will focus here on how the conditions for initiation of shearing cracks may depend on the pitch angle $\Delta\theta$.

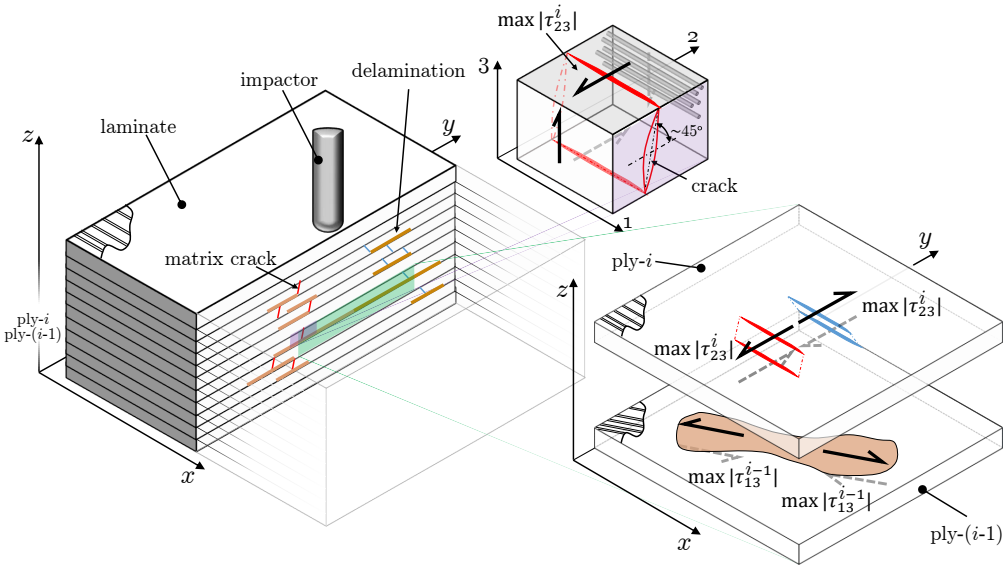

Figure 7: Schematic of the failure mechanisms taking place in the bulk of a laminate composite under out-of-plane loading. Firstly, shearing matrix cracks will form in a generic ply-i due to the intra-laminar τ_{23}^i shear stress. Subsequently, a delamination at a given interface between two plies, $(i-1)$ and i, can form from two cracks driven by the intra-laminar τ_{23}^i shear stress of the ply above and the intra-laminar τ_{13}^{i-1} shear stress of the ply below the interface [16].

In each ply-i, shearing cracks are caused by the τ_{23}^i shear stress component (in material coordinates, see Figure 7). Therefore, in each ply-i, if shearing cracks are to form, we expect them to be located at the point(s) corresponding to maxima of $|\tau_{23}^i|$ (it will be shown later that there are two per ply). Additionally, we know that dynamic effects are not essential for determining damage initiation in LVI [19]. Therefore, the effect of the pitch angle $\Delta\theta$ on the expected locus for the shearing matrix cracks can be inferred from the locus of the maxima of $|\tau_{23}^i|$ in a suitable static linear elastic finite element model.

At the interface between two generic plies $(i-1)$ and i, Choi *et al.* [16] showed that delamination formation starting from shearing cracks in LVI loading conditions is due to $|\tau_{23}^i|$ in the ply-i (ply above) and $\left|\tau_{13}^{i-1}\right|$ in the ply-$(i-1)$ (ply below) (Figure 7). Delaminations then grow aligned with the fibre direction of the ply below [16, 19–21] as schematically illustrated in Figure 7, and hence we know that $\left|\tau_{13}^{i-1}\right|$ plays a significant role in delamination growth for the interface between plies $(i-1)$ and i. Therefore, the effect of the pitch angle $\Delta\theta$ on the expected lo-

cus for delamination at the interface between plies $(i-1)$ and i can in principle be inferred from the maxima of $|\tau_{23}^{i}|$ and $\left|\tau_{13}^{i-1}\right|$ in a suitable static linear elastic finite element model.

4.2.2. FE model

We created five static linear elastic models, one for each pitch angle $\Delta\theta$, using the FE software Abaqus [22]. Both geometries of the laminate and the indenter were the same as the ones used in actual testing conditions. The material properties assigned to each lamina are reported in Table 3. We used conventional quadratic shell elements (S8R) to model the laminate (ply-by-ply using lamination theory) and an analytical surface for the indenter. We conducted a mesh convergence study in order to guarantee a good representation of the elastic response to transverse load of the sample tested. To this end, we used four parameters in order to determine the minimum element size in the impact region: (i) distribution of maximum τ_{13}, (ii) distribution of maximum τ_{23}, (ii) location of points with maximum τ_{23} and (iv) location of points with maximum τ_{23}. The mesh of the impact region converged at a minimum element size of 0.06 mm. We then discretised the laminate with a bias mesh. The four edges of the laminate were simply supported and a vertical downward displacement of 2 mm was applied to the indenter.

4.2.3. FE results and analysis

For each ply-i, Figure 8 shows the likely location of shearing cracks, i.e. points with maximum $|\tau_{23}^{i}|$. In each ply-i, $|\tau_{23}^{i}|$ exhibits two identical maximum values (Figure 8a). The locus of points with maximum $|\tau_{23}^{i}|$ form a double helix, which can be observed in Figure 8b to 8f for $\Delta\theta = 2.5°, 5°, 10°, 20°$ and $45°$ respectively. The double helices are symmetric about the laminate symmetry plane and are better defined for smaller $\Delta\theta$. When observed perpendicularly to the plane of the laminate, all helices corresponding to different $\Delta\theta$ collapse on the same circle, as shown in Figure 8g.

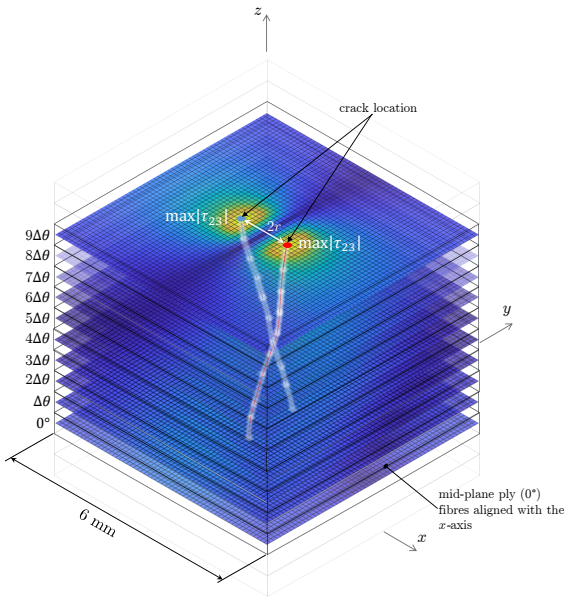

(a) Zoom of the FE model near the impact region, highlighting the double helicoidal distribution in the laminate of the points with $\max|\tau_{23}^i|$ corresponding to the locations of shearing matrix cracks

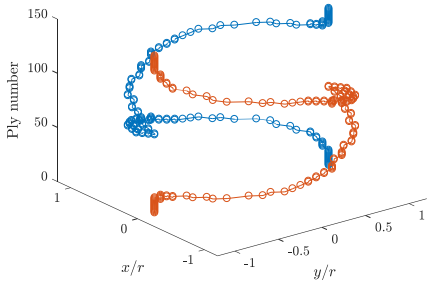

(b) $\Delta\theta = 2.5°$ locus of $\max|\tau_{23}^i|$

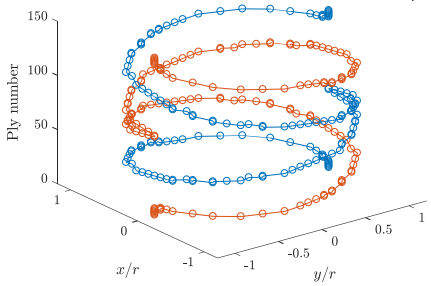

(c) $\Delta\theta = 5°$ locus of $\max|\tau_{23}^i|$

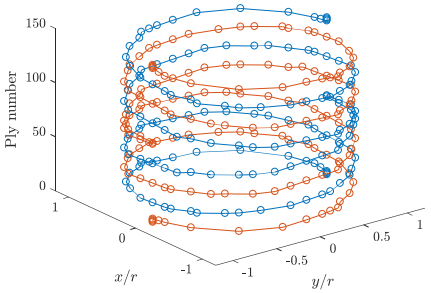

(d) $\Delta\theta = 10°$ locus of $\max|\tau_{23}^i|$

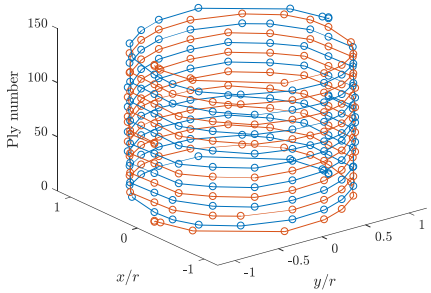

(e) $\Delta\theta = 20°$ locus of $\max|\tau_{23}^i|$

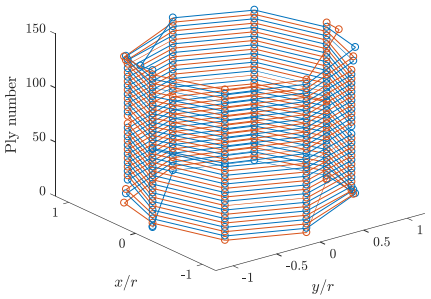

(f) $\Delta\theta = 45°$ locus of $\max|\tau_{23}^i|$

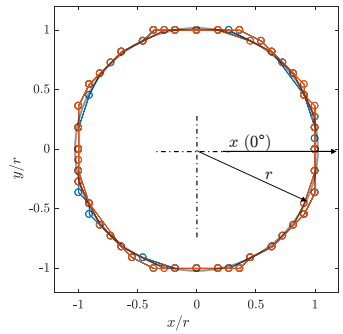

(g) $(x-y)$ projection of $\max|\tau_{23}^i|$ loci (all $\Delta\theta$)

Figure 8: Loci of likely shearing matrix cracks, forming in each ply-i at the locations with $\max|\tau_{23}^i|$, exhibiting a double helicoidal pattern of radius r as $\Delta\theta$ decreases.

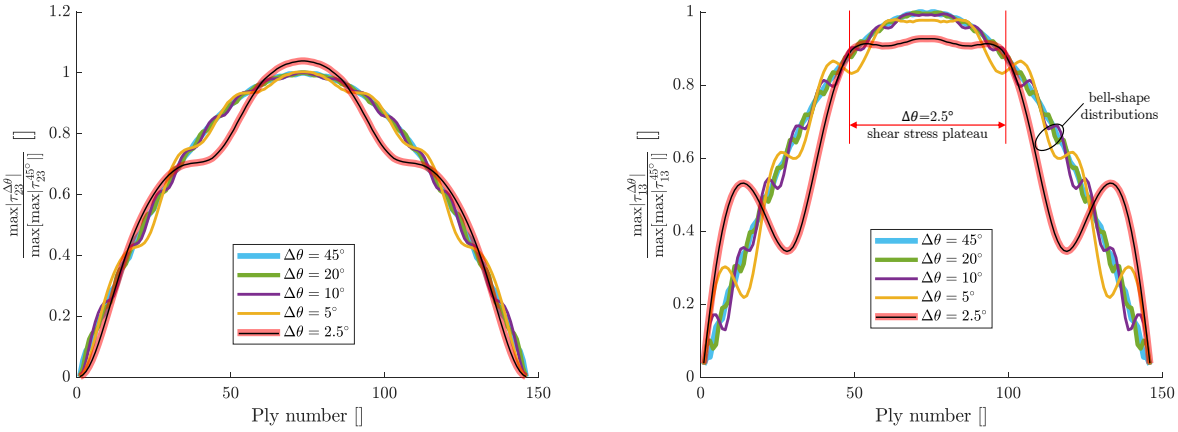

(a) (b)

Figure 9: Through-the-thickness distribution of (a) maximum $|\tau_{23}|$ and (b) maximum $|\tau_{13}|$ for different pitch angles $\Delta\theta$.

Figure 9a shows the through-the-thickness distributions of maximum $|\tau_{23}|$ for laminates with different pitch angles $\Delta\theta$. We normalised each distribution to the highest value of the distribution of maximum $\left|\tau_{23}^{45°}\right|$ in order to highlight the differences between the configurations modelled. Figure 9a shows that for the $\Delta\theta = 2.5°$ configuration, the maximum value of $|\tau_{23}|$ is higher than for any other configurations. This suggests that sub-critical damage (in the form of matrix cracks) should occur earlier for the $\Delta\theta = 2.5°$ configuration; this is consistent with the experimental observation of early loss of linearity observed in the $\Delta\theta = 2.5°$ laminates (see Figure 3a).

Delaminations can potentially initiate from the predicted shearing cracks (see Section 4.2.1). The analysis of the synergistic effect between τ_{23} and τ_{13} in promoting delaminations in configurations with different pitch angles $\Delta\theta$ can be reduced to the study of two consecutive plies, $(i-1)$ and i, and their interface. To this effect, Figure 10a shows a generic ply-i, together with ply-$(i-1)$ at an angle $-\Delta\theta$. For ply-i, Figure 10a shows the $|\tau_{23}^{i}|$ field, and highlights the two locations where $|\tau_{23}^{i}|$ has a maximum and hence shearing cracks are expected to occur. For ply $(i-1)$, Figure 10a shows the $\left|\tau_{13}^{i-1}\right|$ field specifically for $\Delta\theta = 2.5°$, and highlights (for various possible values of $\Delta\theta$) the two locations where $\left|\tau_{13}^{i-1}\right|$ has a maximum and hence where the conditions for delamination growth from a shearing crack are

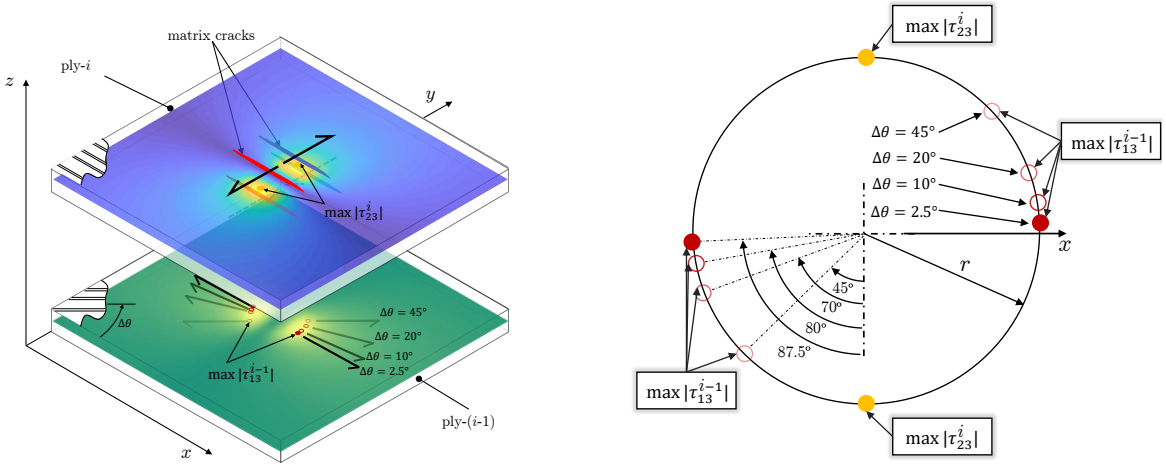

(a) (b)

Figure 10: Synergistic effect between the maximum values of $|\tau_{23}^{i}|$ in the ply-i above, and $\left|\tau_{13}^{i-1}\right|$ in the ply-$(i-1)$ below a given interface for $\Delta\theta = 2.5°, 10°, 20°$ and 45°. (a) Schematic of the two consecutive plies i and $(i-1)$. Two shearing cracks are illustrated in the ply i, located at the points with maximum $|\tau_{23}^{i}|$ (yellow dots). The red dots in the ply $(i-1)$ correspond to the location of maximum $\left|\tau_{13}^{i-1}\right|$ for different pitch angles $\Delta\theta$. (b) Projection of the points illustrated in Figure 10a in the plane of the laminate.

ideal.

Figure 10b shows a projection of Figure 10a on the plane of the laminate, showing that the locus of maximum $|\tau_{13}|$ projects to the same circle corresponding to the projection of maximum $|\tau_{23}|$ shown in Figure 8g. Importantly, Figure 10b shows that the distance between the maximum $\left|\tau_{13}^{i-1}\right|$ and maximum $|\tau_{23}^{i}|$ decreases as the pitch angle $\Delta\theta$ increases. Therefore, increasing the pitch angle $\Delta\theta$ is expected to promote the growth of delaminations from shearing cracks.

Figure 9b shows the thorough-the-thickness distribution of maximum $|\tau_{13}|$ for laminates with different pitch angles $\Delta\theta$. We normalised each distribution to the highest value of the distribution of maximum $\left|\tau_{13}^{45°}\right|$ in order to highlight the differences between the configurations modelled. While the curves for most values of $\Delta\theta$ exhibit a bell shape, it can be observed that, for $\Delta\theta = 2.5°$, there is a substantial plateau. Importantly, the existence of this plateau means that, for $\Delta\theta = 2.5°$, several interfaces will undergo similar maximum shear stresses. This correlates well with the diffused delaminations through the thickness of the laminates with

pitch angle $\Delta\theta = 2.5°$ observed experimentally (Figures 4e and 4f).

Additionally, for laminates with large pitch angles, such as $\Delta\theta = 45°$, delaminations are expected to localize near the few interfaces with maximum $|\tau_{13}|$ and therefore, firstly at the mid-plane of the laminate. This correlates well with the large delamination at the mid-plane of the laminate observed experimentally (Figures 4a). Furthermore, once this central delamination has grown significantly, given the high periodicity of configurations with large pitch angles $\Delta\theta$, a similar analysis for each half of the laminate leads to the expectation of delaminations at the one- and three- quarter height of the laminate, and this is also observed experimentally (Figures 4a).

4.2.4. On the role of pitch angle and ply thickness during the growth of twisting Bouligand-like cracks from the distal face.

In Sections 4.2.1-4.2.3 we have investigated the role of pitch angle $\Delta\theta$ on the formation of shearing matrix cracks and delaminations in Bouligand CFRP thin-ply laminates subjected to low velocity impact. In this section, we will discuss the role of the pitch angle $\Delta\theta$ and ply thickness t_{ply} on the energy release rate for the growth of twisting Bouligand-like cracks forming at the back face of the laminate (LVI tests) due to the tensile stresses originating from bending.

In this context, twisting crack models [23] can be particularly helpful, and therefore we implemented the recent model developed by Suksangpanya *et al.* [9, 10]. This model analyses local stress intensity factors along the crack front of a continuously twisting crack in a Bouligand medium, starting from an initially flat crack, see Figure 11. In our case, this flat crack represents a matrix split at the back face due to the tensile stresses originating from bending. The crack front is initially aligned with the coordinate system (X, Y, Z), with the origin of the coordinate system located at the crack front, and where the X-axis defines the initial crack growth direction and the Y-axis is normal to the initial crack plane. In our problem, the Z-axis therefore coincides with the fibre direction at the initial crack

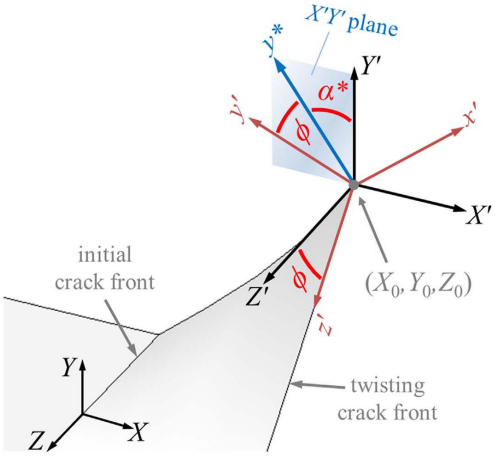

Figure 11: Schematic of a twisting crack in a Bouligand structure initiating from a flat crack, adapted from [9].

front. As the crack grows, kinks and twists, see Figure 11, the local coordinate system of the crack front at any given time is (x', y', z'). Again, in our problem, the z'-axis therefore coincides with the local fibre direction at the current crack front. Figure 11 shows that the twisting of the crack front can be defined by the angle ϕ between Z and z', and, for a fibre-reinforced laminate with individual ply thickness t_{ply}, it is given by

$$\phi = X\left(\frac{\Delta\theta}{t_{\text{ply}}}\right). \tag{1}$$

In addition, the kinking of the crack is defined by the effective kink angle α^*, defined as the angle between y^* and Y', where y^* is obtained by rotating y' about X' by an angle -ϕ (Figure 11). For a fibre-reinforced laminate with individual ply thickness t_{ply}, it is can be expressed as (based on [9]):

$$\alpha^* = \cos^{-1}\left\{\frac{\cos\phi[1+\tan^2\phi]}{\sqrt{[(Z\Delta\theta/t_{\text{ply}})\sec^2\phi]^2+1+\tan^2\phi}}\right\}. \tag{2}$$

To obtain a solution to the energy release rate for the problem described, Suksangpanya *et al.* [9] assume the following: (i) the helicoidal crack grows in an isotropic elastic medium (which is only approximately correct in our case); (ii) the crack front along the twisted path remains straight; (iii) other competing fail-

ure mechanisms such as delaminations and fibre breaks do not occur (which in our case neglects interaction with shearing cracks starting in the bulk of the laminate); and (iv) the flat crack is loaded in mode I with a stress intensity factor K_I (which is representative of the loading condition for bending matrix cracks forming at the back face of the laminate under LVI tests).

Based on this, the energy release rate G at each point on the twisting crack front, normalised to the energy release rate if the crack were to remain flat (G_0), is [9]

$$\frac{G}{G_0} = \left(\frac{k_I^{'}}{K_I}\right)^2 + \left(\frac{k_{II}^{'}}{K_I}\right)^2 + \frac{1}{1-\nu}\left(\frac{k_{III}^{'}}{K_I}\right)^2, \tag{3}$$

where ν is the Poisson's ratio of the isotropic medium, and the local stress intensity factors along the crack front $k_I^{'}$, $k_{II}^{'}$ and $k_{III}^{'}$ are expressed as [9]

$$\frac{k_I^{'}}{K_I} = \cos\left(\frac{\alpha^*}{2}\right)\left[\cos^2\left(\frac{\alpha^*}{2}\right)\cos^2\phi + 2\nu\sin^2\phi\right], \tag{4a}$$

$$\frac{k_{II}^{'}}{K_I} = \sin\left(\frac{\alpha^*}{2}\right)\cos^2\left(\frac{\alpha^*}{2}\right)\cos\phi, \tag{4b}$$

$$\frac{k_{III}^{'}}{K_I} = \cos\left(\frac{\alpha^*}{2}\right)\sin\phi\cos\phi\left[\cos^2\left(\frac{\alpha^*}{2}\right) - 2\nu\right]. \tag{4c}$$

For the design of Bouligand CFRP laminates, the parameters used to tailor the microstructure are the pitch angle $\Delta\theta$ and the ply thickness t_{ply}. For each of the five configurations used in this study, Figures 12a-12b show the energy release rate during crack growth, where it can be seen that the energy release rate for a twisting crack decreases with increasing pitch angle $\Delta\theta$. This result suggests that bending cracks should propagate more easily towards the bulk of the laminate for small pitch angles than for large pitch angles. This is in good agreement with the experimental observations conducted in this work, where the smallest pitch angle $\Delta\theta = 2.5°$ showed helicoidal damage forming at sub-critical levels diffused throughout the entire thickness of the laminate (Figure 4e) and delayed catastrophic failure (load-drop in Figure 3).

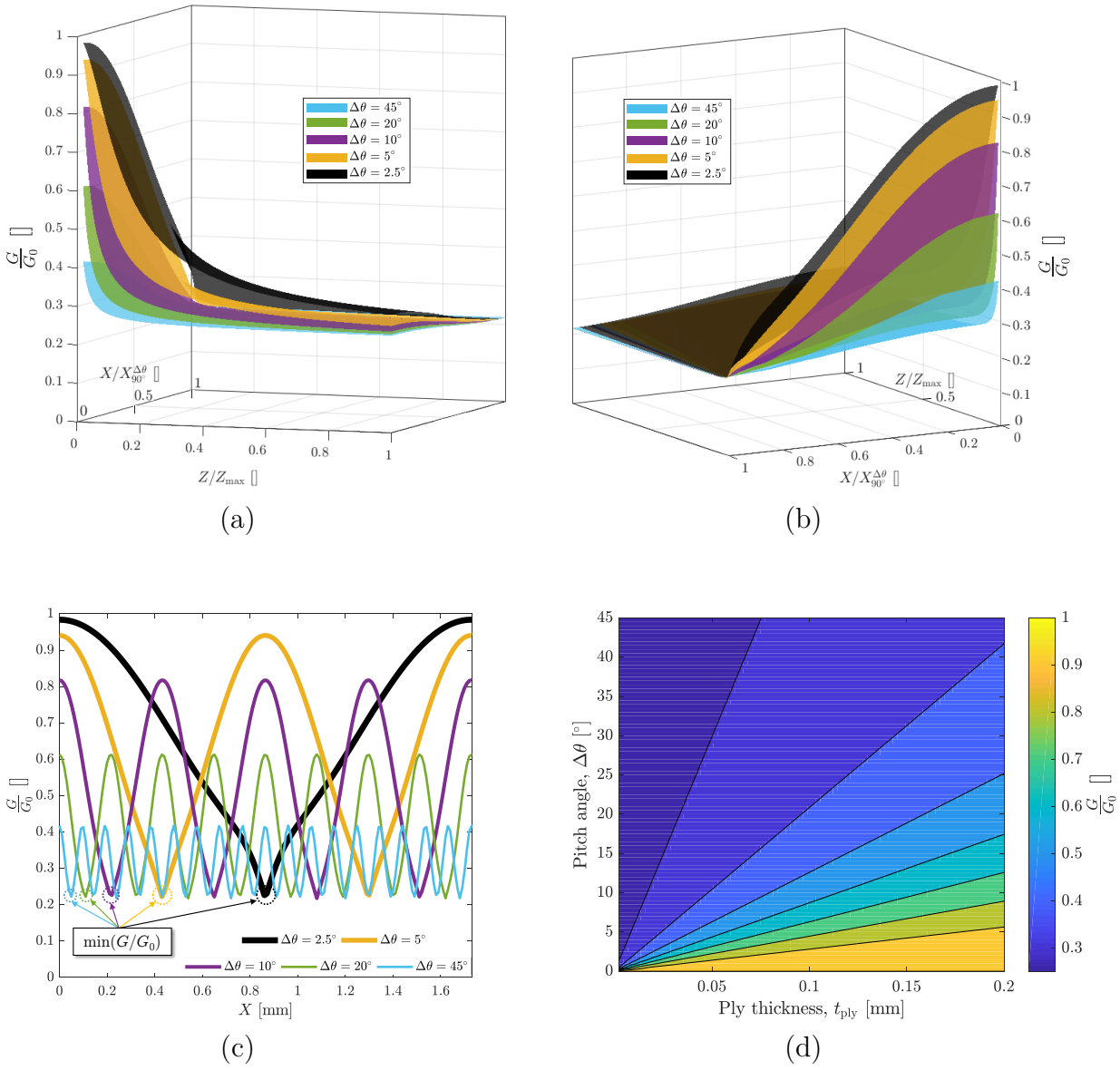

Figure 12: (a-b) Energy release rate maps (G/G_0) describing the crack growth of twisting cracks at each point (X, Z) of the twisting crack path for the pitch angles $\Delta\theta = 2.5°, 5°, 10°, 20°, 45°$ and $t_{\text{ply}} = 0.024$ mm. For each pitch angle $\Delta\theta$, X has been normalised to the value of X with minimum G/G_0. Z has been normalised to half of the crack length. (c) Energy release rate (G/G_0) vs. X evaluated at $Z = 0.1$ mm for the pitch angles $\Delta\theta = 2.5°, 5°, 10°, 20°, 45°$ and $t_{\text{ply}} = 0.024$ mm. (d) Distribution of energy release rate (G/G_0) at (X, Z)=(0,1) as a function of pitch angle $\Delta\theta$ and ply thickness t_{ply}.

Additionally, Figure 12c shows that for decreasing pitch angles $\Delta\theta$, the first local minimum of G/G_0 (circles in Figure 12c), corresponding to a twisting crack front perpendicular to the initially flat crack, is delayed to larger values of X. This also suggests that smaller pitch angles would more easily propagate towards the bulk

of the laminate diffusing sub-critical damage at the back face of the laminate, as observed experimentally (Figure 4e).

The lower energy release rate for twisting cracks, i.e. higher twisting-crack resistance, shown by larger pitch angles (Figure 12a-12b) potentially leads to bending cracks which do not propagate towards the bulk of the laminate, leading to the anticipated activation of more catastrophic mechanisms of failure such as delaminations and fibre breaks. This is in good agreement with the experimental observations conducted in this work where the configurations with pitch angles $\Delta\theta = 20°$ and $45°$ showed localised large delaminations (Figures 4a and 4b), extensive back-face damage (Figure 5c and 5d) and anticipated catastrophic failure (load-drop in Figure 3).

Figure 12d shows G/G_0 as a function of $\Delta\theta$ and t_{ply} with $X = 0$ and $Z = 1$ mm (the curves are qualitatively similar for other points along the crack path). The figure also shows that the energy release rate for twisting cracks increases with ply thickness (for a constant pitch angle $\Delta\theta$). This is in good agreement with other works in the literature on LVI tests of quasi-isotropic laminates (similar to the $\Delta\theta = 45°$ configuration tested in this work) [17, 18]; in these works, it is shown that, as t_{ply} increases (with interply angle and total laminate thickness kept constant), the damage in the bulk of the laminate and the one forming at the back face start interacting.

Based on these observations, we surmise that helicoidal cracks should propagate more easily from matrix splits at the distal face for lower pitch angles (as verified in the experiments) and for larger ply thicknesses.

4.3. On the role of the pitch angle $\Delta\theta$ and the percentage of 0°-ply on the CAI residual properties

Figures 6a and 6b show that, by reducing the pitch angle $\Delta\theta$, similar residual compressive strength and failure strain can be achieved with a decreasing number of 0°-plies (i.e. with fewer plies aligned with the loading direction).

It is known that the CAI strength increases with the proportion of 0°-plies (i.e.

with the proportion of plies aligned with the loading direction) [24, 25]. However, Figures 6a and 6b show that, by reducing the pitch angle $\Delta\theta$, similar residual compressive strength and failure strain can be achieved with a decreasing number of 0°-plies (i.e. with fewer plies aligned with the loading direction). Specifically, we were able to preserve a similar CAI strength and failure strain while reducing the proportion of 0°-plies very significantly from 26% to 2.7%.

5. Conclusions

We investigated several bio-inspired Bouligand thin-ply CFRPs laminates with pitch angles ranging from $\Delta\theta = 2.5°$ to 45°. We conducted LVI and CAI tests to study the influence of the pitch angle $\Delta\theta$ on the damage morphology and mechanical response of the laminate. The main conclusions of this study are here summarized.

The $\Delta\theta = 2.5°$ configuration better mimicked the damage evolution of the Bouligand microstructure of the mantis shrimp's dactyl club, showing:

- enhanced impact damage tolerance obtained via a significant diffused sub-critical damage accumulation before the peak load;
- a smooth and diffused double helicoidal pattern of delaminations;
- a delay in the occurrence of fibre failure at the distal face. This delay may be related to the formation of the double helicoidal delamination pattern; and
- a 13.3% higher peak load and a 34.9% larger displacement at load drop during impact with respect to the single $\Delta\theta = 45°$ test.

In our tests, reducing the pitch angle from $\Delta\theta = 45°$ to $\Delta\theta = 2.5°$ leads to:

- a progressively smoother double helicoidal evolution of damage during impact;
- a more homogeneous distribution of delamination area through most interfaces during impact;
- a statistically-significant reduction of impact damage in the form of delamination, with a 29.4% decrease in total projected delamination area ($p-$value $=$ 0.005), a 35.8% decrease in delamination extent ($p-$value $=$ 0.007) and a

46.8% decrease in extent of back-face damage ($p-$value $= 0.037$); and

- similar residual properties both in terms of CAI strength ($p-$value $= 0.11$) and CAI failure strain ($p-$value $= 0.1$), achieved with a progressively smaller amount of 0°-plies (26% of plies aligned with the loading direction for $\Delta\theta = 45°$ while only 2.7% for $\Delta\theta = 2.5°$).

We created FE models of the biomimetic thin-ply CFRP laminates to analyse the role of the pitch angle $\Delta\theta$ on triggering different damage mechanisms, as observed experimentally. For this, the analysis of the intra-laminar shear stress τ_{23} allowed us to infer the distribution of shearing matrix cracks in laminates with different pitch angles $\Delta\theta$. Subsequently, we analysed the conditions for the formation of delaminations initiating from the matrix cracks focusing on the intra-laminar τ_{13} and τ_{23} shear stresses. The main conclusions are the following:

- the points in the laminate where shearing matrix cracks are predicted to initiate are distributed in a double helicoidal progressively better defined as the pitch angle $\Delta\theta$ decreases;
- the $\Delta\theta = 2.5°$ configuration shows a higher maximum value of τ_{23} than any of the other configurations. This might have led to an anticipated formation of sub-critical damage in the $\Delta\theta = 2.5°$ configuration (in the form of matrix cracks) resulting in the early loss of linearity observed in the experimental mechanical response;
- the synergistic effect between τ_{13} and τ_{23} in promoting delaminations decreases as the pitch angle decreases. This will have contributed to delaying delamination initiation for $\Delta\theta = 2.5°$; and
- the $\Delta\theta = 2.5°$ configuration shows similar maximum τ_{13} values for a large number of plies. This is expected to promote the failure of several interfaces, thereby generating diffused delamination damage (as experimentally observed in $\Delta\theta = 2.5°$ laminates).

We analysed how the pitch angle $\Delta\theta$ and the ply thickness t_{ply} affect the resistance of Boulignad CFRP composites to growing twisting Bouligand-like cracks

forming at the back face of the laminate (LVI tests) due to the tensile stresses originating from bending. The main conclusions are the following:

- by reducing the pitch angle $\Delta\theta$, the crack resistance (under dominant Mode I opening) to growing Bouligand cracks decreases, facilitating the propagation of sub-critical matrix cracks forming at the back-face towards the bulk of the laminate. This is in good agreement with the largely diffused sub-critical helicoidal damage observed in the $\Delta\theta = 2.5°$ configuration;
- by increasing the pitch angle $\Delta\theta$, the crack resistance (under dominant Mode I opening) to growing Bouligand cracks increases, promoting the occurrence of catastrophic mechanisms of failure, such as delaminations and fibre breaks. This is in good agreement with the localised large delaminations, extensive fibre failure and the anticipated catastrophic failure observed in configurations with large pitch angles such as $\Delta\theta = 20°$ and $45°$.

With the progressive use of automated tow/tape placement in large-scale engineering applications, which in principle enable the large-scale use of Bouligand microstructures, the benefits of Bouligand structures demonstrated in this paper can in principle find widespread use in industrial practice.

Acknowledgements:

The funding from the European Union's Horizon 2020 research and innovation programme under the Marie Sklodowska-Curie grant agreement No. 722626 (FibreMod, www.fibremodproject.eu) is gratefully acknowledged.

References

[1] Y. Bouligand, Twisted fibrous arrangements in biological materials and cholesteric mesophases, Tissue and Cell 4 (1972) 192–217.

[2] T. Apichattrabrut, K. Ravi-Chandar, Helicoidal composites, Mechanics of Advanced Materials and Structures 13 (2006) 61–76.

[3] L. Cheng, A. Thomas, J. L. Glancey, A. M. Karlsson, Mechanical behavior of

bio-inspired laminated composites, Composites Part A: Applied Science and Manufacturing 42 (2011) 211–220.

[4] L. K. Grunenfelder, N. Suksangpanya, C. Salinas, G. Milliron, N. Yaraghi, S. Herrera, K. Evans-Lutterodt, S. R. Nutt, P. Zavattieri, D. Kisailus, Bio-inspired impact-resistant composites, in: Acta Biomaterialia, volume 10, pp. 3997–4008.

[5] J. S. Shang, N. H. Ngern, V. B. Tan, Crustacean-inspired helicoidal laminates, Composites Science and Technology 128 (2016) 222–232.

[6] F. Pinto, O. Iervolino, G. Scarselli, D. Ginzburg, M. Meo, Bioinspired twisted composites based on Bouligand structures, in: Proc. SPIE 9797, Bioinspiration, Biomimetics, and Bioreplication 2016, Las Vegas, Nevada, US, p. 97970E.

[7] D. Ginzburg, F. Pinto, O. Iervolino, M. Meo, Damage tolerance of bio-inspired helicoidal composites under low velocity impact, Composite Structures 161 (2017) 187–203.

[8] J. L. Liu, H. P. Lee, V. B. C. Tan, Failure mechanisms in bioinspired helicoidal laminates, Composites Science and Technology 157 (2018) 99–106.

[9] N. Suksangpanya, N. A. Yaraghi, D. Kisailus, P. Zavattieri, Twisting cracks in Bouligand structures, Journal of the Mechanical Behavior of Biomedical Materials 76 (2017) 38–57.

[10] N. Suksangpanya, N. A. Yaraghi, R. B. Pipes, D. Kisailus, P. Zavattieri, Crack twisting and toughening strategies in Bouligand architectures, International Journal of Solids and Structures 150 (2018) 83–106.

[11] C. Gloor, Spooky - Smashing Mantis Shrimp, Flickr, www.flickr.com, accessed on 07/08/2018 (2015).

[12] J. C. Weaver, G. W. Milliron, A. Miserez, K. Evans-Lutterodt, S. Herrera, I. Gallana, W. J. Mershon, B. Swanson, P. Zavattieri, E. DiMasi, D. Kisailus, The stomatopod dactyl club: A formidable damage-tolerant biological hammer, Science 336 (2012) 1275–1280.

[13] G. Bullegas, S. T. Pinho, S. Pimenta, Engineering the translaminar fracture behaviour of thin-ply composites, Composites Science and Technology 131 (2016) 110–122.

[14] ASTM D7136/D7136M-15 Standard Test Method for Measuring the Damage Resistance of a Fiber-Reinforced Polymer Matrix Composite to a Drop-Weight Impact Event, in: ASTM International, 2015.

[15] ASTM D7137/D7137M-17 Standard Test Method for Compressive Residual Strength Properties of Damaged Polymer Matrix Composite Plates, in: ASTM International, 2017.

[16] H. Y. Choi, f. K. Chang, A Model for Predicting Damage in Graphite/Epoxy Laminated Composites Resulting from Low-Velocity Point Impact, Journal of Composite Materials 26 (1992) 2134–2169.

[17] T. Yokozeki, A. Kuroda, A. Yoshimura, T. Ogasawara, T. Aoki, Damage characterization in thin-ply composite laminates under out-of-plane transverse loadings, Composite Structures 93 (2010) 49–57.

[18] A. Wagih, P. Maimí, E. V. González, N. Blanco, J. R. De Aja, F. M. De La Escalera, R. Olsson, E. Alvarez, Damage sequence in thin-ply composite laminates under out-of-plane loading, Composites Part A: Applied Science and Manufacturing 87 (2016) 66–77.

[19] S. Abrate, Impact on Laminated Composite Materials, Applied Mechanics Reviews 44 (1991) 155.

[20] D. Liu, Impact-Induced Delamination—A View of Bending Stiffness Mismatching, Journal of Composite Materials 22 (1988) 674–692.

[21] M. Richardson, M. Wisheart, Review of low-velocity impact properties of composite materials, Composites Part A: Applied Science and Manufacturing 27 (1996) 1123–1131.

[22] Dassault Systemes ®, Abaqus FEA 6.14 - Simulia™, 2018.

[23] K. T. Faber, A. G. Evans, Crack deflection processes-I. Theory, Acta Metallurgica 31 (1983) 565–576.

[24] L. Reis, M. de Freitas, Damage growth analysis of low velocity impacted composite panels, Composite Structures 38 (1997) 509–515.

[25] A. T. Nettles, S. Sabo, Compression after impact strength of thin laminates with various percentage of 0° plies, Journal of Composite Materials 48 (2014) 345–354.

[26] J. D. Fuller, M. R. Wisnom, Pseudo-ductility and damage suppression in thin ply CFRP angle-ply laminates, Composites Part A: Applied Science and Manufacturing 69 (2015) 64–71.

[27] Composite Oracle, Pyrofil TR30S 3K, Composite Oracle, www.composite-oracle.com, accessed on 23/01/2019 (2019).

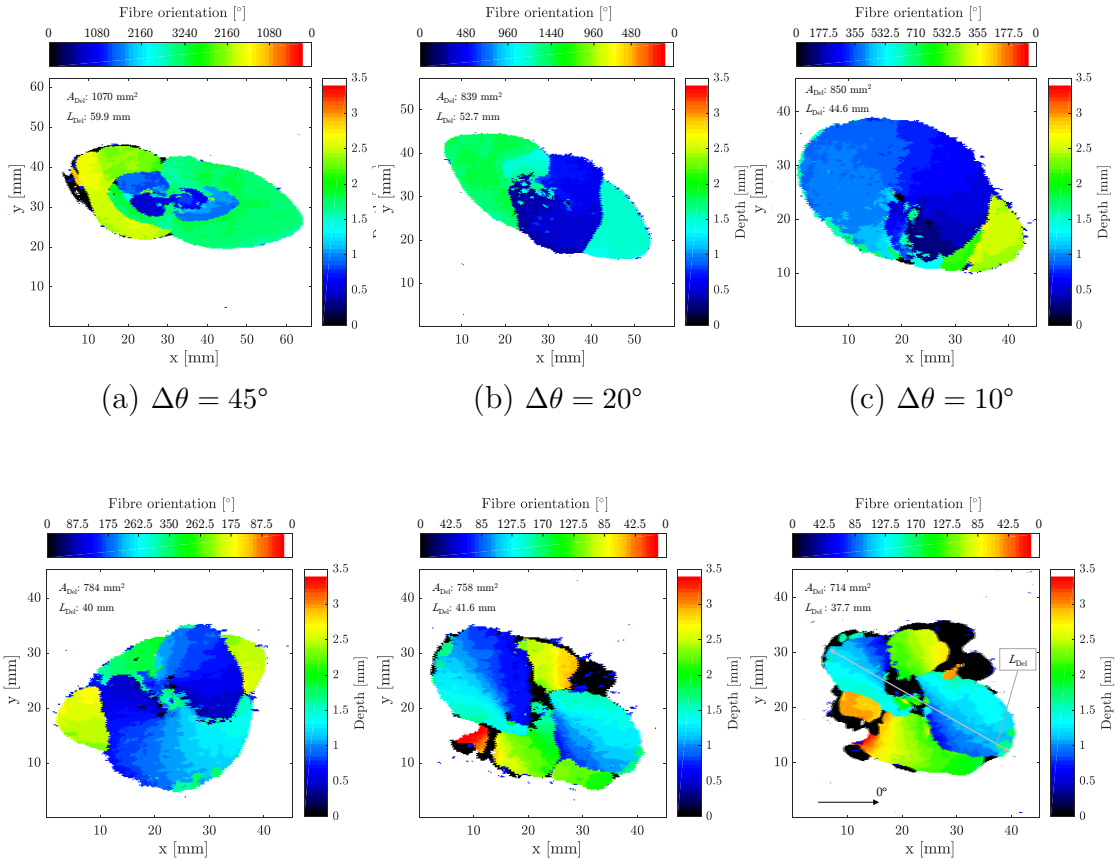

(a) $\Delta\theta = 45°$ (b) $\Delta\theta = 20°$ (c) $\Delta\theta = 10°$

(d) $\Delta\theta = 5°$ (e) $\Delta\theta = 2.5°$ sample 2 (f) $\Delta\theta = 2.5°$ sample 1

Figure 13: Zoom-in of ultrasonic C-scan of impacted (LVI) laminates. The coloured areas indicate the presence of delamination. The colour scheme, blue (impact side) - red (distal face), correspond to different locations of the delamination through the thickness of the laminate.